Earth Planet. Sci. Lett. 636 (2024) 118713

Contents lists available at ScienceDirect

Earth and Planetary Science Letters

journal homepage: www.elsevier.com/locate/epsl

The effect of aqueous fluid on viscous relaxation of garnet and modification of inclusion pressures after entrapment

Xin Zhong [a,*], David Wallis [b], Phillip Kingsbery [a], Timm John [a]

[a] Institut für Geologische Wissenschaften, Freie Universität Berlin, Malteserstrasse 74–100, 12449 Berlin, Germany
[b] Department of Earth Sciences, University of Cambridge, Cambridge, CB2 3EQ, UK

ARTICLE INFO

Keywords:
Thermobarometry
Raman spectroscopy
EBSD
Mineral inclusions
Viscous relaxation

ABSTRACT

The elastic interaction between an inclusion and its host is often employed to study metamorphic processes based on the assumption that the host is not affected by processes such as creep that irreversibly releases stress. However, it is not well understood how fast inelastic relaxation of stress may occur and under what conditions the elastic regime holds for each inclusion-host system. To provide new constraints for the widely used systems of quartz and zircon inclusions in garnet, we performed heating experiments on almandine-pyrope and spessartine garnets under graphite, N_2+H_2, or H_2O+Ar fluxed conditions at different temperatures. Raman spectroscopy was used to measure the same quartz and zircon inclusions after different heating times. The Raman-band wavenumbers undergo time-dependent decreases in quartz inclusions and increase in zircon inclusions under H_2O+Ar conditions and exhibit a greater final shift than under graphite and N_2+H_2 buffered conditions. Under graphite-buffered conditions, the wavenumbers of Raman bands measured on zircon and quartz stabilise after the first heating step, after which no change was observed. Electron backscatter diffraction results reveal greater misorientation around the heated inclusions compared to unheated inclusions, implying a greater dislocation density after heating. Raman mapping reveals that stress heterogeneity in the garnet host develops at an early stage of heating and fades away afterward, indicating dispersal of dislocations into the host. Fitting a visco-elastic model to the Raman data of garnet fluxed with N_2+H_2 or Ar+H_2O allows an estimate of flow-law parameters for garnet around quartz inclusions, similar to those obtained by conventional deformation experiments. The results demonstrate the weakening effect of aqueous fluid on garnet. The data also indicate that the garnet can hold inclusion pressure at elevated temperatures under a dry and reducing environment. This study provides information on the relaxation rate of pressurized inclusions in garnet at different temperatures and within different external environments. Furthermore, the use of inclusion-host pairs for studying creep processes offers a complementary approach to conventional deformation experiments to better understand the rheological behaviour of earth materials.

1. Introduction

Pressure and temperature (*P-T*) are critical variables in the reconstruction of geological histories of metamorphic and magmatic rocks. Elastic thermobarometry is a method for estimating *P-T* conditions that has been extensively used in recent petrological studies (e.g. Bayet et al., 2020; Cisneros et al., 2022; Gonzalez et al., 2021). When a mineral inclusion was entrapped by a host at depth, its pressure is assumed to be equal to that of the host. Due to the different elastic compressibilities and thermal expansivities of the inclusion and host, the inclusion will develop a different pressure than the host upon any *P-T* changes (Angel et al., 2017b; Gillet et al., 1984; Guiraud and Powell, 2006; Moulas et al., 2020; Rosenfeld and Chase, 1961; Zhang, 1998; Zhong et al., 2021). After exhumation, a residual pressure will be preserved in an entrapped inclusion, which can be measured with Raman spectroscopy (e.g., Enami et al., 2007). Using an elastic model, it is therefore possible to obtain constraints on the entrapment pressure and temperature (Angel et al., 2017b; Guiraud and Powell, 2006; Kohn, 2014; Zhang, 1998). The application of elastic thermobarometry relies on accurate determination of the equation of state (EoS) of both the mineral inclusion and host at high *P-T* conditions (Angel et al., 2017a, 2022), and the system must remain in the elastic regime. Meanwhile, several corrections have been

* Corresponding author.
E-mail address: xinzhong0708@gmail.com (X. Zhong).

https://doi.org/10.1016/j.epsl.2024.118713
Received 15 May 2023; Received in revised form 20 March 2024; Accepted 11 April 2024
Available online 27 April 2024

investigated to account for complicating effects, such as the inclusion shape (Mazzucchelli et al., 2018), inclusion depth (Mazzucchelli et al., 2018; Zhong et al., 2019b), and elastic anisotropy of the inclusion (Murri et al., 2018; Stangarone et al., 2019) or the host (Gonzalez et al., 2021). The method has been experimentally tested by synthesizing inclusion-host systems, such as quartz-in-garnet (e.g. Bonazzi et al., 2019; Thomas and Spear, 2018), and has been applied in many petrological and tectonic studies (Ashley et al., 2014; Bayet et al., 2018; Groß et al., 2020; Kohn, 2014; Moulas et al., 2020; Schwarzenbach et al., 2021; Szczepański et al., 2021; Taguchi et al., 2019). Inclusions of different thermo-elastic moduli in the same sample have also been used to constrain metamorphic histories (Baldwin et al., 2021; Gilio et al., 2022; Zhong et al., 2019a).

Garnet, commonly considered as a strong metamorphic mineral with a high yield stress (Karato et al., 1995), serves as an ideal vessel for containing up to gigapascal-levels residual pressure of its inclusions. However, a common observation made while applying quartz-in-garnet elastic barometry, especially in regional studies, is that quartz inclusions in the same sample may record significantly different residual pressures, even though no explanation can be found based on microscale factors, such as elongated shape, cracks, or proximity to the thin-section surface/bottom (e.g., Bayet et al., 2020; Cisneros et al., 2022; Groß et al., 2020). Considering that in a coherent geological unit with the same lithology spatially close samples should have experienced a similar metamorphic *P-T* history, the question arises whether the modification of the residual pressures of the inclusions is only related to elastic anisotropy, inclusion shape, or inclusion depth, or whether it is related heterogeneous strength, and hence localised weakness, of the host.

Although garnet is considered a strong mineral, it can creep under differential stress, particularly at elevated temperatures (e.g., Karato et al., 1995; Wang and Ji, 1999; Xu et al., 2013). Therefore, a critical prerequisite for inferring the metamorphic *P-T* conditions using an entrapped inclusion is that the inclusion pressure has not been modified by creep, which leads to an irreversible stress release often at elevated temperature after a certain deformation time (e.g. Karato, 2012). The creep rate of garnet is a function of time and temperature, but other factors, such as fluid influx, affecting the behavior of the host-inclusion system might also be important. It is well known that aqueous fluids are common in metamorphic systems (e.g., Austrheim, 1987; Kaatz et al., 2022; Putnis and John, 2010; Wayte et al., 1989) and may weaken nominally anhydrous minerals (Kaatz et al., 2023; Kohlstedt, 2006; Wayte set al., 1989; Xu et al., 2013). Therefore, it is important to quantify whether fluid influx has a significant impact on the efficiency of stress relaxation in inclusion-host systems. Such constraints may allow determination of whether an inclusion pressure has been modified to achieve an accurate geological interpretation. In this study, we performed high-*T* experiments on natural garnets that contain quartz and zircon inclusions under various buffering conditions to study the rate of viscous relaxation of the garnet host. Variations in relaxation rate under the different conditions demonstrate that the garnet host can be substantially weakened by adding small amounts of water in the surrounding environment, which drastically speeds up relaxation of the inclusion pressure. The results provide important guidance for practical applications of elastic thermobarometry and chronometry using relaxed inclusion pressures in future works.

2. Sample and analytical method

2.1. Samples

Two samples were utilized for experiments. The first sample is an eclogite collected from the Adula nappe, Ticino, Switzerland (Swiss coordinate 732,180, 135,623). This sample contains mainly garnet, omphacite, quartz and plagioclase. Abundant quartz, zircon and rutile inclusions, along with minor apatite, are present in the garnet. The garnets are chemically zoned with cores of $Alm_{0.43}Grs_{0.24}Prp_{0.32}Sps_{0.01}$ and rims of $Alm_{0.47}Grs_{0.16}Prp_{0.36}Sps_{0.01}$ (Fig. S1). The second garnet sample is a spessartine from Sangulungulu, Loliondo, Tanzania. The crystal is approximately 1 cm in diameter, occurs in a mica schist, and is orange in colour with good transparency. Abundant zircon inclusions are present. The garnet composition is $Alm_{0.03}Grs_{0.06}Prp_{0.14}Sps_{0.77}$ and is spatially homogeneous according to point analyses performed at different locations in the garnet (Table S1). Both samples were polished on one side with 0.25 μm diamond suspension and subsequently cut into slices about 200 μm thick and 1 cm^2 in area to make the inclusions visible under transmitted light for experimental purposes.

2.2. Heating experiments

Heating experiments were performed using a Gero furnace. The ceramic furnace tube was sealed with rubber rings and metal lids. The experiments were performed under three sets of conditions. One set of experiments was performed under graphite-buffered conditions maintained by placing the sample in a ceramic crucible filled with pre-dried graphite and fluxing the tube with Ar gas. The graphite and sample were heated to 400 °C with Ar gas flux for a few hours before setting to the target temperature. A second set were performed under N_2+H_2 (5 vol% H_2) fluxed conditions. A third set were performed under H_2O+Ar gas fluxed conditions, in which Ar gas first went through a reservoir of demineralized water maintained at approximately 75 °C. The gas flux rate was approximately 10 L/hour measured by a flowmeter. The concentration of H_2O carried by the Ar gas was determined to be around 10 wt% by measuring the weight loss of H_2O and the total Ar gas flux after approximately 1 hour (supplementary Fig. S2).

The samples were heated, taken out and measured for the inclusion pressures with Raman spectroscopy, and this procedure was repeated. The number of heating steps and heating duration were chosen to observe sufficient modification of the final residual inclusion pressure of quartz and zircon compared to the initial one. To avoid the α-β quartz transition at high temperature, temperatures and heating time were chosen to keep the calculated inclusion pressure above the pressure of the transition. The localities of quartz and zircon inclusions were recorded before heating so that the same inclusions could be remeasured after heating. The heating ramp of the furnace was set at 300 °C/h. After the experiment, cooling of the furnace was assisted by the gas flow. Starting from a temperature of 900 °C, the temperature dropped below 600 °C within one hour.

The oxygen fugacities, f_{O_2}, of the three buffering conditions were calculated with FactSage (Bale et al., 2016). Between 750 °C and 900 °C, the graphite buffered experiments provided f_{O_2} between $10^{-20.9}$ Pa and $10^{-19.2}$ Pa, the N_2+H_2 buffer provided between $10^{-22.4}$ Pa and $10^{-19.0}$ Pa, and the H_2O+Ar buffer provided between $10^{-7.4}$ Pa and $10^{-6.3}$ Pa (supplementary Fig. S4). Therefore, the three experiments span a wide range of oxygen fugacity with the H_2O+Ar buffer providing an extreme oxidizing environment and the graphite and N_2+H_2 buffers providing reducing environments. For the N_2+H_2 fluxed conditions, a test was performed by heating metallic iron powder for 20 h at 900 °C. The results indicate that the oxygen fugacity is indeed below the iron-wüstite transition (i.e., below $\log_{10}(f_{O_2}) \approx -17$) as no wüstite nor magnetite was detected by powder X-ray diffraction (XRD) (supplementary Fig. S5). However, when water was added into the N_2+H_2 gas, magnetite was formed as detected by XRD (Fig. S5).

2.3. Raman spectroscopy

A WiTec Alpha300-R confocal Raman spectrometer at the Freie Universität Berlin was used in this study. Zeiss EC Epiplan 50X/0.75 and 100X/0.95 objectives were used to measure inclusions. A polarized solid-state laser was used with a wavelength of 532.1 nm. The laser energy output was set to < 8 mW to avoid laser heating (see supplementary Fig. S6). A UHTS300 VIS spectrometer with a grating of 1800 grooves/mm and a 1650-lines CCD area detector was used with a

spectral range from 85 to 1254 cm^{-1}. By measuring the full-width-half-magnitude (FWHM) of the peaks from a Hg/Ar calibration lamp, we estimated the spectral resolution to be approximately 1.5 cm^{-1}. A silicon plate was used to calibrate the Raman-band position every hour and the variation was less than 0.2 cm^{-1} (supplementary Fig. S7). Data processing and inclusion selection criterion follow Zhong et al. (2019a). Gem-quality quartz and zircon crystals were used as stress-free reference material with reference spectra given in supplementary Fig. S8. The integration time was approximately 5–10 s with 5 to 20 repetitions. For mapping, the integration time was 4–10 s for each pixel and the spatial resolution was 0.5 μm, resulting in maps of 60×60 pixels across a 30×30 μm area. After the heating experiments, some inclusions had developed cracks around them and were therefore not measured. During mapping, the laser focus was set slightly above the central plane of the quartz inclusion to carry more signal from garnet. The residual pressures of the inclusions were calculated based on the shifts of the 464 cm^{-1} band for quartz and 1008 cm^{-1} band for zircon compared to the stress-free gem-quality quartz and zircon crystal following the hydrostatic calibration from Schmidt et al. (2013); Schmidt and Ziemann (2000). The non-hydrostatic stress tensor is later calculated using the calibration from Reynard and Zhong (2023), where it was found that the 206 cm^{-1} band position is only sensitive to the mean stress while the other bands such as the 464 and 128 cm^{-1} bands are more sensitive to differential stress. Therefore, the calibration requires using the band shift of the 464 cm^{-1}, 206 cm^{-1} pair or the 128 cm^{-1}, 206 cm^{-1} pair to simultaneously calculate the mean stress and differential stress assuming symmetry in the basal plane.

2.4. Electron-probe microanalysis (EPMA)

A JEOL JXA 8200 Superprobe at the Freie Universität Berlin was used to determine the chemical composition of garnet, using the wavelength-dispersive detectors. The instrument was operated at an acceleration voltage of 15 kV and beam current of 120 nA. The elements Si, Al, Fe, Mg, Ca, Mn, Ti and Cr were analysed. The dwell time was 60 ms and the spatial increment was 1 μm. Quantitative point analyses were made on the core, mantle, and rim of the garnet and the relationship between photon intensity and the element concentration is obtained using the ZAF correction.

2.5. Electron backscatter diffraction

Electron backscatter diffraction (EBSD) data were acquired on a FEI Quanta 650 field-emission gun scanning electron microscope fitted with a Bruker eFlash HD detector. Diffraction patterns were obtained at the full 1600×1200 resolution of the detector at a specimen tilt of 70°, accelerating voltage of 30 kV, and working distance of 27.7 mm. Step sizes were in the range 0.3–0.7 μm and maps contained between 52,470 points and 205,800 points. Three maps were obtained from a sample of the eclogite that had not undergone heat treatment. Three maps were obtained from a sample heated to 820 °C for 218 h in Ar + H_2O gas. Two maps were obtained from a sample heated to 900 °C for 41 h in Ar + H_2O gas. The MTEX toolbox for MATLAB® was used to plot maps of the garnet host coloured by the misorientation angle of each pixel relative to the average orientation of the garnet within each map area (Bachmann et al., 2010).

2.6. Numerical model

A radially-symmetric visco-elastic model is applied to simulate the stress evolution of quartz and zircon inclusions upon heating at atmospheric confining pressure in an infinite garnet host (Zhong et al., 2020). A finite-difference solver was employed in MATLAB to solve the system of equations given in the supplementary materials. To simulate the experiment, three steps are considered, that is (1) the stress build-up during the initial heating ramp, 2) the visco-elastic relaxation process at the maximum temperature, and 3) the stress modification during cooling. The first and third processes can be approximated as purely elastic due to the fast heating and cooling rates and lower average temperatures. The second process needs to be treated with a visco-elastic model. To simulate time-dependent viscous relaxation of stress at high temperature, the viscosity of the host garnet is needed. The viscosity is assumed to be non-Newtonian and is defined as $\eta = A|\tau_{rr}|^{1-n}$, where τ_{rr} is the radial deviatoric stress, A is a pre-factor and n is the stress exponent, which is set as 3 (Wang and Ji, 1999; Xu et al., 2013). The equation of state for quartz is from Angel et al. (2017b), that of zircon is from Ehlers et al. (2022) and the endmembers of garnet is from Angel et al. (2022). The PVT relation is averaged based on the molar proportions of garnet endmembers. The outcome of the model is a predicted *P-T-t* path of the inclusion during the heating-relaxation-cooling sequence. At the end, the only variable, that is the pre-factor for viscosity, can be inversely determined by fitting the modelled results and measured Raman data with Newton's method. The model considers isotropic inclusion in isotropic host, thus only the mean stress (pressure) is needed. The fitted viscosity pre-factor is used to calculate the characteristic timescale, t, of viscous relaxation following the equation presented by Dabrowski et al. (2015), that is $t = \frac{4n}{3(n-1)}\frac{\mu}{K}$, where the effective viscosity $\mu = \frac{A}{2}(P_{inc}/n)^{1-n}$, K is the bulk modulus of the inclusion, and the inclusion pressure, P_{inc}, is taken to be 1 GPa. This characteristic time is derived assuming a viscous and incompressible host.

3. Results

3.1. Raman spectroscopy results

Examples of the Raman spectra from quartz and zircon inclusions are given in Fig. 1. This sample was heated to 868 °C with Ar+H_2O gas. The Raman-band wavenumbers exhibit a time-dependent increase for zircon inclusions and decrease for quartz inclusions. The FWHM of the 910 cm^{-1} band in garnet is shown in Fig. 2 to monitor the garnet stability. The FWHM remains unchanged after the applied heating duration under H_2O+Ar fluxed conditions. The bulk composition of garnet and shape of the inclusions did not show noticeable changes by checking with EPMA and optical microscope, respectively. Furthermore, no new Raman peaks were found after heating. Therefore, the garnets did not break down within the duration of heating.

In Fig. 3, the Raman shift with respect to the original peak position in the unheated sample is plotted against heating time for each inclusion. The 464 cm^{-1} band of quartz and the 1008 cm^{-1} band of zircon are the most intense and strongly affected by the stress/strain (Murri et al., 2018; Reynard and Zhong, 2023; Schmidt et al., 2013; Schmidt and Ziemann, 2000; Stangarone et al., 2019), thus they are chosen to monitor the rate of viscous relaxation. In the graphite buffered experiments performed at temperatures between 750 °C and 900 °C (Fig. 3a), the position of the 464 cm^{-1} band of most quartz inclusions drops by less than 1 cm^{-1} and stabilizes after approximately 50 h. The position of the 1008 cm^{-1} band of zircon increases by about 1.0, 1.5, and 2.3 cm^{-1} when heated to temperatures of 750 °C, 820 °C, and 900 °C, respectively. Little change in peak position occurs after the first heating stage in either quartz or zircon in the graphite buffered experiments.

Under N_2+H_2 fluxed conditions (Fig. 3b), the wavenumbers of the 464 cm^{-1} Raman band measured on quartz inclusions exhibit slightly more time-dependent decrease that was ongoing at the end of the set of experiments. Under the same conditions, the wavenumber of the 1008 cm^{-1} Raman band in zircon increases by about 2 cm^{-1} and 3.5 cm^{-1} at temperature 820 and 900 °C, respectively, and then remains approximately constant. For the 750 °C experiment, the difference of the relative shift between quartz and zircon is too small to separate them.

Under the H_2O+Ar fluxed conditions (Fig. 3c), a continuous shift in the position of the 464 cm^{-1} band of quartz occurs across all heating times and at each temperature. The rate of wavenumber shift with time

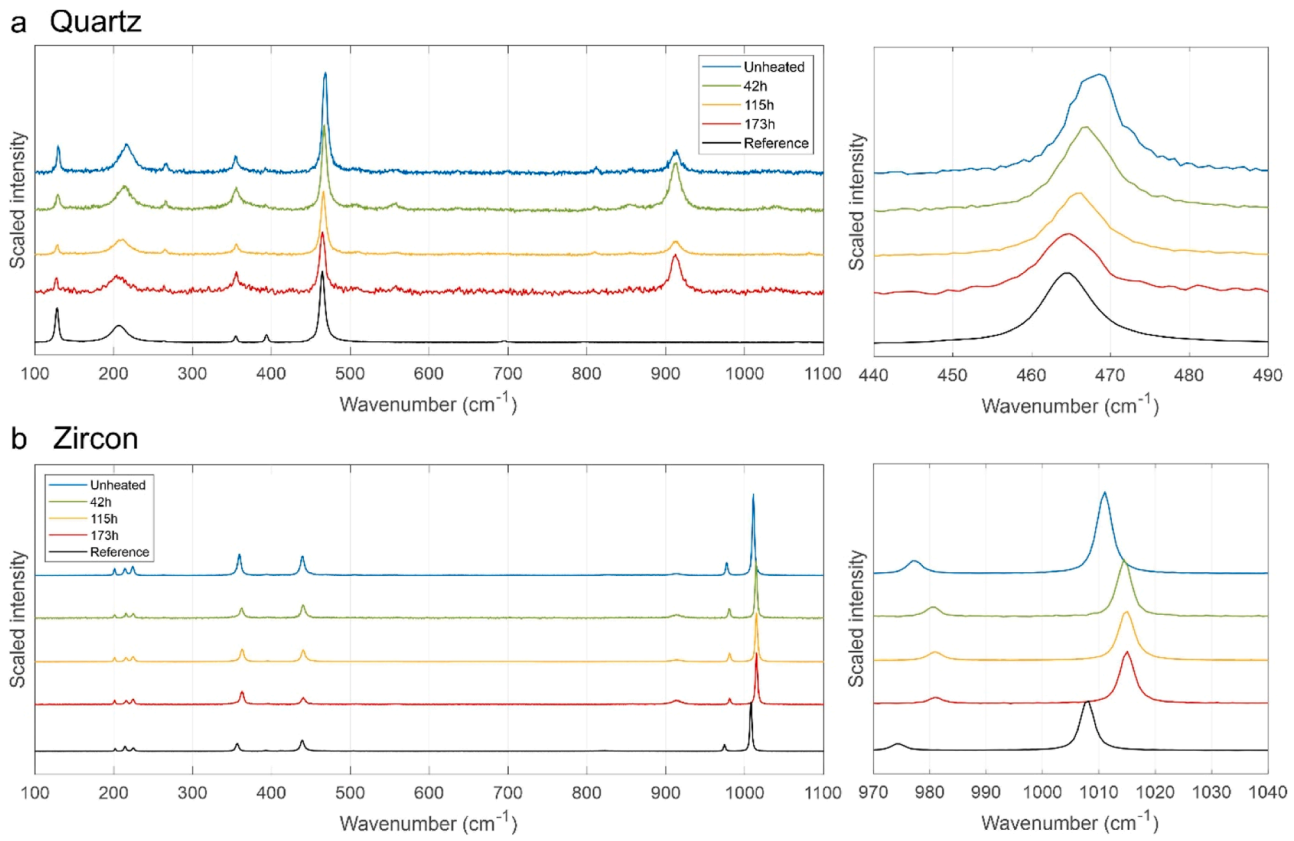

Fig. 1. Raman spectra of a quartz and a zircon inclusion in garnet measured at room temperature after different amounts of heating time. The experimental temperature for the shown data is 868 °C with Ar + H_2O gas. The black curves show the spectra from reference stress-free quartz and zircon crystal.

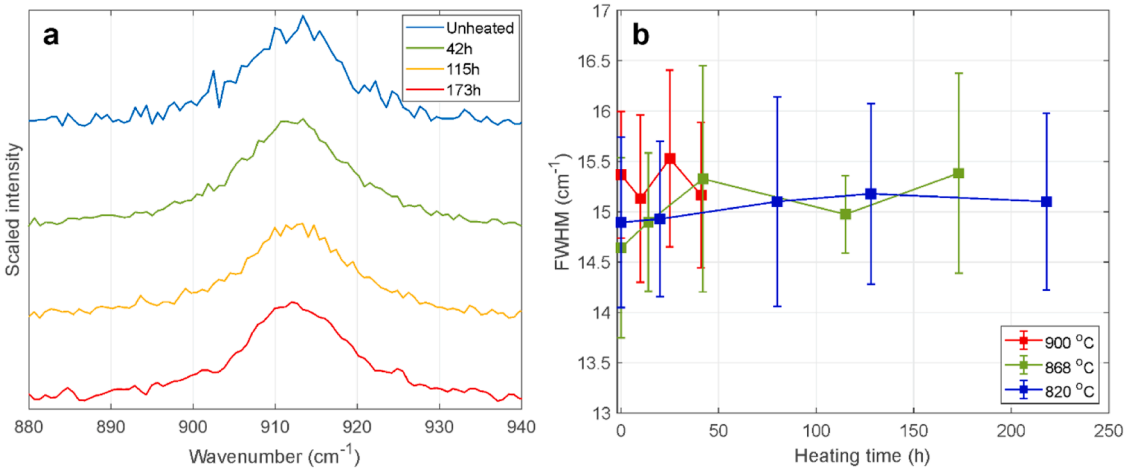

Fig. 2. **a**. Raman spectra (910 cm^{-1} band) of garnet host measured at the same location after different heating durations at 868 °C under H_2O+Ar fluxed condition (H_2O+Ar gas fluxed). **b**. The FWHM of garnet around measured quartz and zircon inclusions. The mean value and 1-σ are calculated based on the FWHM of all spectra (about 10–30 points) after each duration of heating.

increases with temperature across the three sets of experiments. At 820 °C the wavenumber of this band shifts by about −1 cm^{-1} after approximately 220 h (about 4.5 × 10^{-3} cm^{-1} per hour). At 868 °C and 900 °C the wavenumber of the band shifts by about −2 cm^{-1} to −3 cm^{-1} over shorter durations, giving rates of approximately 1.7 × 10^{-2} cm^{-1} per hour and 5 × 10^{-2} cm^{-1} per hour (Fig. 3b). The experiment performed at 750 °C shows less shift after 200 h heating compared to those at the higher temperatures. For zircon, the wavenumber of the 1008 cm^{-1} band increases most rapidly during the early stages of heating before converging to a plateau. The time taken for the 1008 cm^{-1} wavenumber to stabilise at a constant value decreases with increasing temperature.

For spessartine garnet, only the H_2O+Ar buffered condition is applied (Fig. 3d). No quartz inclusion was found in spessartine garnet. The relative Raman shift is less than the eclogite garnet, possibly due to composition difference. The dashed line (Fig. 3c and 3d) indicates the modelled results assuming complete reset at experimental temperature, i.e. inclusion and host are fully reset to room pressure at experimental temperature and rapidly brought to room temperature. For spessartine (Fig. 3d), the match is good in comparison to the eclogite garnet (Fig. 3c). Potential reasons for the mismatch, e.g. excess volume, is

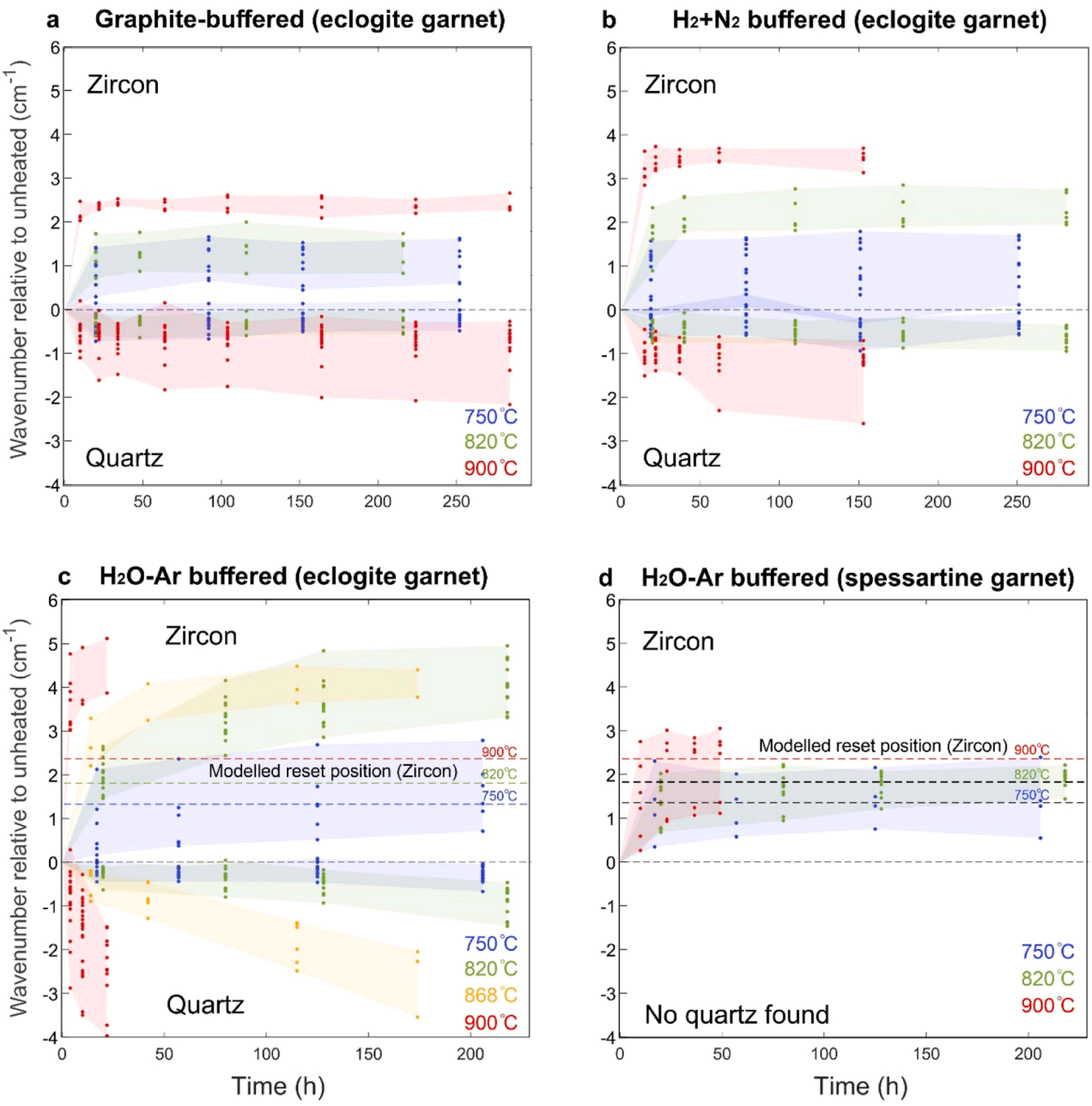

Fig. 3. Time-dependent shifts in Raman band position of quartz and zircon inclusions. **a, b** and **c** present the results from graphite buffered, H_2+N_2 and H_2O+Ar gas buffered experiments on eclogite garnet. **d** shows the H_2O+Ar fluxed condition performed on Tanzania spessartine garnet. Zircon and quartz data are plotted together, with zircon having positive shifts (wavenumber increases compared to that of the unheated sample) and quartz having negative shifts. The dashed lines in **b** and **d** show the numerically modelled Raman band position if complete viscous reset occurs. In the plot, each dot represents an inclusion measured after different heating time compared to its unheated state. The peak position's uncertainty is <0.1 cm^{-1} by monitoring a Si standard (Fig. S7).

discussed in supplementary materials.

Fig. 4 summarises the final wavenumber shifts that occurred under each buffer. For zircon, the three buffering conditions result in separate data clusters at 820 °C and 900 °C, between which the minimum and maximum values of Raman shift are separated, and the shifts progressively increase across the graphite, N_2+H_2, and H_2O+Ar buffers. At 750 °C, the difference among the three buffering conditions is too small to be completely separated. For quartz, the three data clusters are not completely separated, potentially due to the heating times not being sufficiently long, but the trend in the absolute magnitudes of the shifts across the three different buffers is similar to that from zircon.

Raman mapping of quartz inclusions before and after heating shows that inclusion shapes did not change significantly as shown in Fig. 5 and Fig. S9. The 910 cm^{-1} band of garnet and 464 cm^{-1} band of quartz inclusions are shown to test for stress/strain heterogeneity. The wavenumber of the 464 cm^{-1} band in quartz inclusions decreases continuously in all three cases. For garnet, initially, the spatial distribution of the wavenumber of the 910 cm^{-1} band is heterogeneous with variation on the order of 1 cm^{-1}. After heating, the heterogeneity in the shift of the 910 cm^{-1} band is increased to about 2–3 cm^{-1}. The increase in heterogeneity is most pronounced after 115 h at 868 °C (Fig. 5a) and 17 h at 900 °C (Fig. 5c). After longer heating times, the heterogeneity starts to decrease and the pattern of the shift in the 910 cm^{-1} band is more homogeneous after 174 h and 60 h for these two cases, respectively. Three profiles across the garnet demonstrate the temporal variation of the 910 cm^{-1} band position. The maps and profiles of shifts in

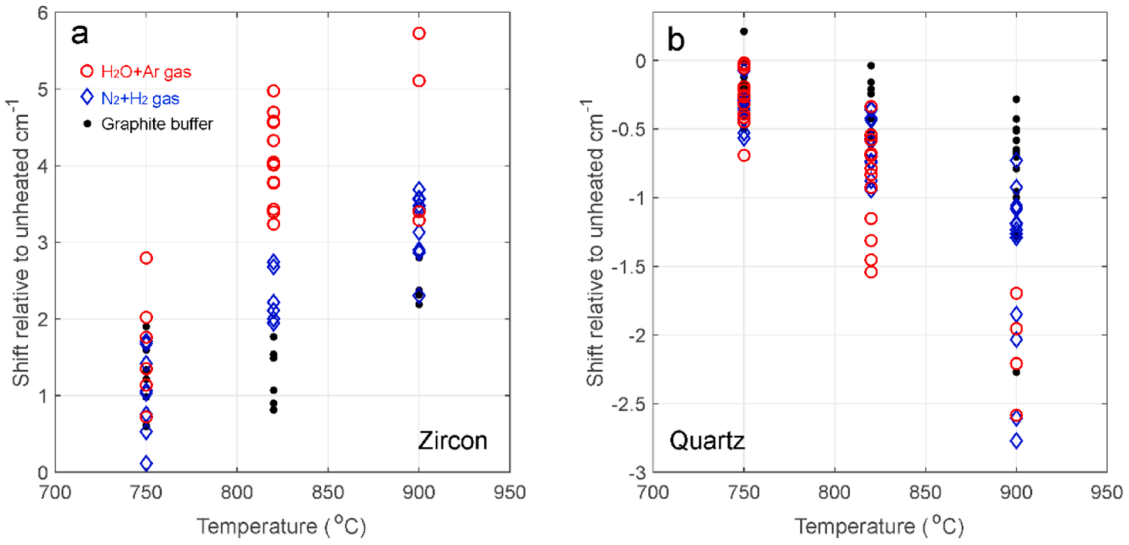

Fig. 4. Comparison of Raman band position at different buffering conditions. The *y*-axis denotes the variation of Raman band position of the 1008 cm^{-1} band for zircon (**a**) and 464 cm^{-1} band for quartz (**b**) with respect to the band position prior to heating. Each dot represents an inclusion measured after the last heating time given in Table 1 under different buffering conditions. The peak position's uncertainty is <0.1 cm^{-1} by monitoring a Si standard (Fig. S7).

the 910 cm^{-1} band reveal that the maximum shift generated in the vicinity of the inclusions after heating progressively decreases in magnitude whilst, at the same time, the area of the zone exhibiting shift around the inclusion progressively increases. For example, the position of the Raman band in Fig. 5a is initially at about 911.5 cm^{-1} in the far-field and 913.5 cm^{-1} closer to the inclusion. After 115 h of heating, the wavenumber of the central region close to the inclusion increases to around 915 cm^{-1}. After 174 h, the wavenumber in the central region drops below 913.5 cm^{-1}, while the wavenumber in the far-field region has increased to between 912.5 cm^{-1} and 913 cm^{-1}.

3.2. EBSD results

EBSD results in Fig. 6 show large misorientation angle due to heating. The misorientation represents the angle between the crystal orientation at each pixel point and the average orientation of garnet within the map area. In Fig. 6, the top row presents the misorientation around three quartz inclusions in an unheated eclogite garnet. The second row (820 °C with H_2O+Ar buffer) and the third row (900 °C with H_2O+Ar buffer) present the misorientation around heated quartz inclusions. In general, unheated samples exhibit low magnitudes of misorientation, whereas the heated samples exhibit greater misorientation, typically in the range 0.5–1°, in a patchy distribution. The regions with high misorientation are also typically more concentrated at the narrower tips of the inclusions. There is no significant difference in the distributions of misorientation around inclusions in the samples heated at 820 and 900 °C, potentially due to the longer heating time at 820 °C compared to 900 °C (Table 1). The patchy shape of the misorientated regions is in general similar to the structure evident in the maps of Raman shifts in Fig. 5, where the regions exhibiting significant shift are also distributed rather heterogeneously.

3.3. Numerical modelling results

Examples of modelled *P-T* paths of a quartz inclusion and a zircon inclusion heated to experimental temperature at room pressure are presented in Fig. 7. Upon heating, the quartz inclusion develops higher pressure due to its greater thermal expansivity than that of garnet. At the maximal temperature of 820 °C, the pressure of the quartz inclusion reaches approximately 1.1 GPa. The overpressure decreases as a function of heating time at the maximal temperature. Subsequently, the temperature is brought back to room temperature (25 °C), which results in the final residual pressure being less than the initial residual pressure. The amount of pressure decrease depends on the temperature and time at the maximum temperature.

Similar time-dependent behaviour but with the opposite trend is predicted for zircon in Fig. 7C and 7D. Tensile stress starts to develop at temperatures of 400–500 °C depending on the initial inclusion pressure. The tensile stress is relaxed by viscous deformation at the maximal temperature. This relaxation leads to an increase of the final residual pressure compared to the initial residual pressure. Table 1 presents the best-fit flow-law parameters obtained at different temperatures following the inverse numerical method described in the supplementary material. With the Monte-Carlo method, the uncertainties can be calculated, and the histograms of calculated pre-factor *A* are presented in supplementary Fig. S10. For conceptual comprehension, the pre-factors for viscosity are converted into characteristic timescales of viscous relaxation presented in Fig. 8. A linear trend is observed as expected between $1/T$ and the logarithmic relaxation time. The results of the N_2+H_2 fluxed experiments yield a somewhat close, but slightly longer, characteristic relaxation time compared to those obtained under the H_2O+Ar fluxed conditions. For zircon inclusions, the relaxation time is approximately 2–3 orders of magnitude shorter than those of quartz inclusions.

4. Discussions

4.1. Effects of aqueous fluid on pressure relaxation

In the H_2O+Ar fluxed experiments, oxygen is present due to the absence of a second buffer that absorbs all oxygen. In the N_2+H_2 fluxed experiment, the oxygen fugacity is below that of the iron-wüstite transition. Therefore, the three sets of experiments represent three situations that are 1) hydrogen and oxygen absent (graphite-buffered), 2) hydrogen present but oxygen absent (N_2+H_2 fluxed), and 3) both hydrogen and oxygen present (H_2O+Ar fluxed). This range represents the possible environments that a garnet may encounter during its retrograde path and allows us to identify the individual effects of hydrogen and oxygen on creep.

In the graphite buffered experiment, no time-dependent variation of Raman-band position is observed after the first heating step (Fig. 3). It is speculated that an initial trace amount of water in garnet may exist in

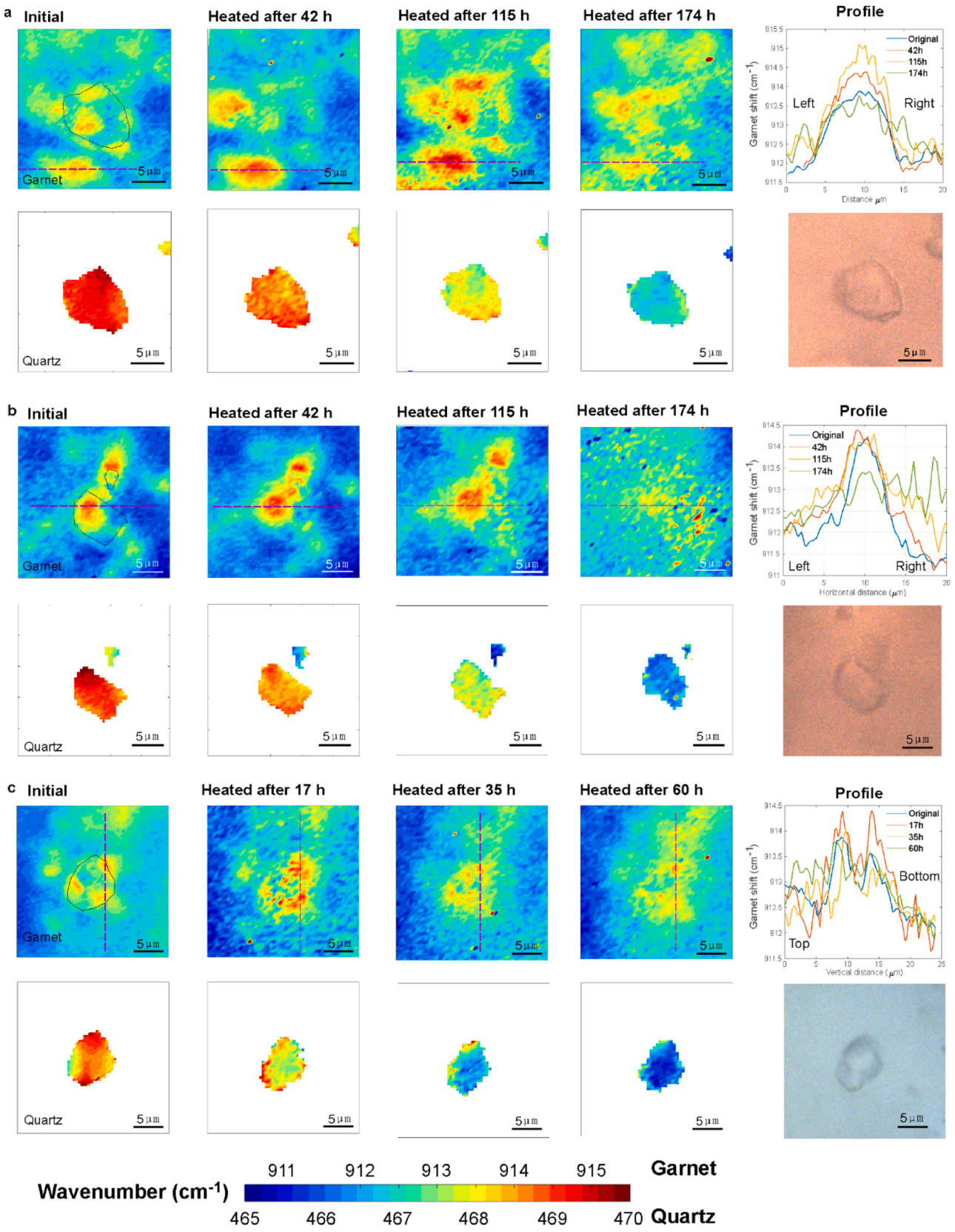

Fig. 5. Raman maps of entrapped quartz inclusions in garnet hosts before and after heating experiments. All three experiments in **a, b** and **c** were performed under H_2O+Ar fluxed condition. The experiments in **a, b** were performed at 868 °C, and that in **c** was performed at 900 °C. Each panel presents the wavenumbers of either the 910 cm^{-1} band in garnet or the 464 cm^{-1} band in quartz. The purple dashed lines denote the location of the profiles plotted on the upper-right side to demonstrate the time-dependent variation of Raman band position in garnet.

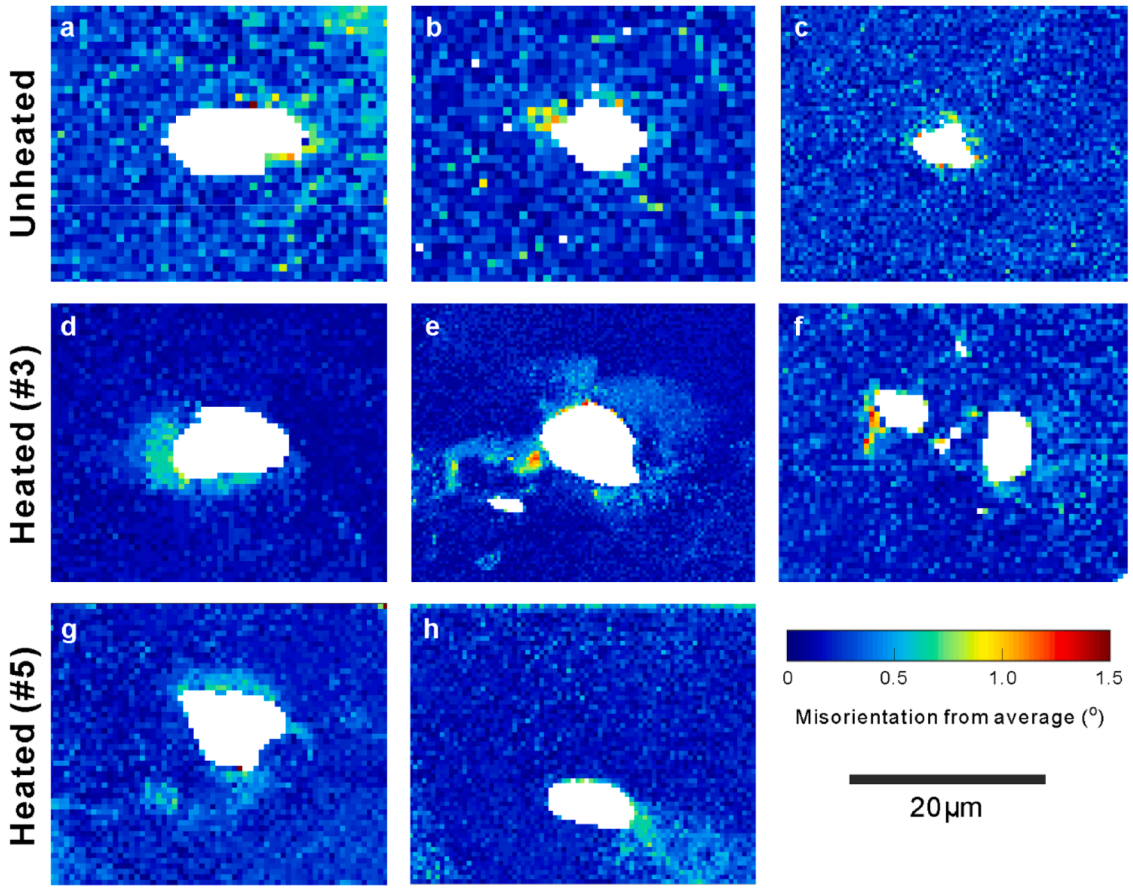

Fig. 6. Misorientation maps from EBSD data. The first row (**a** to **c**) is from an unheated sample. The second and third rows (**d** to **h**) are from heated samples with the heating experiment number indicated to the left. The misorientation is calculated from the average garnet orientation within the domain.

sealed pores, microscale fluid inclusions, or minor inclusions of hydrous mineral. After the first heating step, water is removed from the garnet, leading to the stable Raman-band position.

In the N_2+H_2 fluxed experiment, the rate of stress relaxation for zircon inclusions is faster than under the graphite-buffered conditions but slower than under the H_2O+Ar fluxed conditions at 820 °C condition (Fig. 4). As for quartz inclusions, the difference is much smaller and it is difficult to separate the Raman shift between the graphite-buffered and the N_2+H_2 fluxed experiment due to the large scattering of different inclusions (Fig. 4). A faster relaxation under N_2+H_2 fluxed experiment may be attributed to the presence of extra hydrogen, as it has been suggested that at high temperature hydrogen may enter the lattice and modify the point-defect chemistry in a manner that facilitates dislocation climb in crystal-plastic deformation (Kohlstedt, 2006). However, this effect is rather small, especially for quartz inclusions (ca. 0.2 cm^{-1} shift in mean value compared to >1 cm^{-1} scattering), and may as well be simply due to statistical fluctuation or a small compositional variation of garnet. An explanation for the small effect of hydrogen is that the confining pressure is atmospheric, and the water/hydrogen solubility is very low at low pressure (e.g. Fei and Katsura, 2020). Therefore, more experiments, or ab-initio calculations at higher pressure is needed to quantify the effect of hydrogen on garnet, e.g. as done in the experiments by Xu et al. (2013) for water.

In comparison to hydrogen, the effect of oxygen is based on the results from the H_2O+Ar fluxed experiment showing a linear dependence of residual pressure with respect to heating duration (Fig. 3), and the large variation in Raman shift of heated inclusions as compared to unheated ones (Fig. 4). The effect is also manifested by the greater misorientation around quartz inclusions heated under H_2O+Ar fluxed conditions than around those in the unheated sample (Fig. 6). This difference reflects a greater density of dislocations responsible for the stress relaxation (Nye, 1953; Wallis et al., 2016; Wheeler et al., 2012).

The activation energy can be calculated by fitting the viscosity pre-factor A to the Arrhenius equation $A = A_0 \exp(Q/RT)$, where A_0 is the pre-factor for A and Q is the activation energy. For the quartz-in-garnet system, the activation energy is 263±45 kJ/mol under H_2O+Ar fluxed conditions and 232±80 kJ/mol under N_2+H_2 fluxed conditions, consistent with the reported value for wet garnet of 215±45 kJ/mol (Xu et al., 2013). Our calculated value is lower than the recalculated values of 417±26 kJ/mol from Karato et al. (1995) and 470±65 kJ/mol and Wang and Ji (1999) for dry, almandine-rich garnet. Xu et al. (2013) proposed that the incorporation of hydrogen into garnet is associated with the metal site as $[(OH)_O^{\cdot}] = [H_{Me}^{'}]$, where the Kröger and Vink (1956) notation is used. It is suggested that dislocation climb is rate-limited by the slowest diffusing element, e.g., Si (Kohlstedt, 2006). Xu et al. (2013) has proposed a mechanism explaining the effect of hydrogen on creep rate whereby hydrogen sits on the Si site and the Si diffusivity is increased by increasing water fugacity with an exponent of one. In our data, the water fugacity is not varied and remains substantially lower than the water fugacity tested by Xu et al. (2013), but our calculated activation energy of 263±45 kJ/mol is within error of the value of 215±45 kJ/mol presented by Xu et al. (2013). Within our experimental conditions, oxygen dominants the weakening of garnet. This is based on the observation that Raman peak shift from the H_2O+Ar experiment being much higher than the N_2+H_2 and graphite-buffered experiment. However, the effect of hydrogen is not fully explored in this work due to the low partial pressure of H in the N_2+H_2 environment.

For zircon inclusions, the relaxation time is shorter than that of quartz inclusions by approximately 2–3 orders of magnitude, but the slope with respect to $1/T$ is similar (Fig. 8). This observation is similar to

Table 1
Experimental conditions. The formula for characteristic relaxation time is given in Discussions. The stress exponent n is set to 3 for dislocation creep. Viscous pre-factor A is fitted for 820 to 900 °C experiments and used to calculate the characteristic relaxation time.

No.	Sample	T (°C)	Buffer	Total time (h)	Pre-factor A ($Pa^3.s$)	Relaxation time (h)
#1	Eclogite	750	Graphite + Ar gas	252	N/A	N/A
#2	Eclogite	820	Graphite + Ar gas	210	N/A	N/A
#3	Eclogite	900	Graphite + Ar gas	284	N/A	N/A
#4	Eclogite	750	Ar + H_2O gas	206	N/A	N/A
#5	Eclogite	820	Ar + H_2O gas	218	$10^{35.0 \pm 0.1}$ (a)	$10^{3.8 \pm 0.2}$ (a)
#6	Eclogite	868	Ar + H_2O gas	174	$10^{34.4 \pm 0.1}$ (a)	$10^{3.2 \pm 0.1}$ (a)
#7	Eclogite	900	Ar + H_2O gas	41	$10^{34.1 \pm 0.1}$ (a)	$10^{2.9 \pm 0.1}$ (a)
#8	Spessartine	750	Ar + H_2O gas	206	N/A	N/A
#9	Spessartine	820	Ar + H_2O gas	218	$10^{32.1 \pm 0.4}$ (b)	$10^{\circ.8 \pm 0.4}$ (b)
#10	Spessartine	900	Ar + H_2O gas	49	$10^{31.3 \pm 0.7}$ (b)	$10^{\circ.1 \pm 0.7}$ (b)
#11	Eclogite	750	$N_2 + H_2$ gas(c)	251	N/A	N/A
#12	Eclogite	820	$N_2 + H_2$ gas(c)	281	$10^{35.2 \pm 0.1}$ (a)	$10^{4.0 \pm 0.1}$ (a)
#13	Eclogite	900	$N_2 + H_2$ gas(c)	153	$10^{34.4 \pm 0.2}$ (a)	$10^{3.2 \pm 0.2}$ (a)

(a) is fitted based on quartz inclusion data; (b) is fitted based on zircon inclusion data; (c) the N_2+H_2 gas contains 5 vol% of H_2 and 95 vol% of N_2 (forming gas). For experiment #4~10, the water reservoir is set at the temperature ca. 75 °C. The water solubility in Ar gas is measured and can be found in Fig. S2.

that of Campomenosi et al. (2023), where the pressure of a zircon inclusion was reset nearly instantaneously by continuously heating the garnet. One possibile cause proposed by Campomenosi et al. (2023) is that garnet is weaker under tensile stress than compressive stress around a zircon inclusion. In addition, we checked the FWHM and shift of the 1008 cm^{-1} peak of zircon. Before heating, we did not observe any correlation between the FWHM and shift of the 1008 cm^{-1} peak. After heating, shifts of the 1008 cm^{-1} peak position indicate the increase of residual pressure but no change of FWHM is found (supplementary Fig. S11).

4.2. Time scale of creep versus timescale of diffusion

The characteristic time scale of viscous relaxation of a pressurized quartz inclusion at high temperature is compared to the time scale of chemical diffusion in garnet (Fig. 8). The characteristic diffusion time scale is evaluated using L^2/D, where L is the characteristic length and D is the diffusion coefficient. Characteristic lengths of 10 μm and 100 μm are used as examples to represent the length scales of chemical heterogeneity in garnet. The Fe-Mg exchange diffusion coefficient is calculated with the results from Chakraborty and Ganguly (1992) and Chu and Ague (2015), which are all for dry garnet. The oxygen fugacity is set at the graphite buffer. The diffusion coefficient for Fe-Mg exchange in wet garnet is from Zhang et al. (2019). The Si self-diffusion coefficient in dry garnet is based on Shimojuku et al. (2014), and no equivalent for wet garnet has been reported to our knowledge. Our determined time scale of viscous relaxation is within two orders of magnitude of the characteristic diffusion timescales for Fe-Mg exchange from Chakraborty and Ganguly (1992), Chu and Ague (2015), and Zhang et al. (2019). The determined stress-relaxation timescale is substantially shorter than the characteristic timescale of Si diffusion in dry garnet by approximately four orders of magnitude (Shimojuku et al., 2014).

The timescales for stress relaxation and diffusional exchange of Fe-Mg over distances of 10–100 μm in wet garnet are similar. The petrological implication is that, if water was present and pre-existing chemical zonation in a 10–100 μm garnet has been removed by diffusion, then it is likely that quartz or zircon inclusions will have been reset soon after water entered the system. Under dry conditions at $T < 800$ °C, Si diffusion is about two orders of magnitude slower than that of the metal elements (Fig. 8). If the rate of stress relaxation is limited by the rate of dislocation climb, which in turn is controlled by diffusion of point defects, the measured slower Si diffusion rate would be consistent with our data showing slow stress relaxation under graphite-buffered conditions (Fig. 3a). Such slow relaxation rates will allow inclusions to preserve information on the conditions of their entrapment. To reset the inclusion pressure to the ambient pressure, a higher temperature is required to create more point defects and increase the rate of dislocation motion. It needs to be noted that diffusion length is present in the equation for chemical homogenization time but it is absent in that for viscous relaxation time. For garnet with a different size, adjustment needs to be made for $t = L^2/D$.

3.4. Departure of residual stress from hydrostatic

The significance of elastic anisotropy can be evaluated by calculating the non-hydrostatic residual stress preserved in the inclusions. For quartz inclusions, the residual stress is calculated using two approaches, that is the Grüneisen tensor (Murri et al., 2018) and experimental calibrations (Reynard and Zhong, 2023). For zircon, only the Grüneisen tensor is available (Stangarone et al., 2019). For quartz, the 128, 206 and 464 cm^{-1} peaks are used and for zircon the 439, 975 and 1008 cm^{-1} peaks are used. Due to the symmetry, only σ_a (stress along the a-axis) and σ_c (stress along the c-axis) are needed and the departure from hydrostatic can be evaluated by the differential stress $\sigma_c - \sigma_a$. In Fig. 9, we plot the pressure (negative mean stress) against the differential stress ($\sigma_c - \sigma_a$) for the H_2O+Ar experiment where the shift is more significant compared to the other two buffering conditions. Compressive stress is taken as negative.

For quartz inclusions, the calculated residual differential stress is negative based on the experimental calibration from Reynard and Zhong (2023) with an average of −0.18±0.08 GPa, consistent with numerical modelling results (Mazzucchelli et al., 2019; Reynard and Zhong, 2023). Using the Grüneisen tensor (Murri et al., 2018), the calculated differential stresses span between negative and positive values, and show a wider scattering of 0.28±0.13 GPa, potentially due to the limited number of Raman peaks used. For the differential stress of zircon, a small variation from −0.10±0.05 to −0.18±0.07 GPa is observed after heating. As the difference is within the uncertainty, it is not conclusive whether the magnitude of differential stress increased or not after heating. For both quartz and zircon, the measured differential stress as a proxy for a departure from hydrostatic condition is mostly within 0.2 GPa.

4.3. Geological and geodynamical implications

When extrapolated to lower temperatures around 700 °C, the characteristic timescale of viscous relaxation for quartz inclusions is on the order of 10^5–106 h (about 10–100 years) under H_2O+Ar fluxed conditions. These timescales suggest that if free water was interacting with the rock and hence the garnet for more than 10–100 years during the retrograde evolution at temperatures around 700 °C, it is possible that the inclusion pressure will be reset to the external confining pressure during retrogression. Similarly, at a temperature of 600 °C the characteristic timescale of relaxation is about 1000 years under H_2O+Ar fluxed conditions (Fig. 8). These estimates imply that at these temperatures, to preserve unrelaxed residual pressures that can be used to recover the entrapment pressure, the retrograde evolution needs to be either dry, or

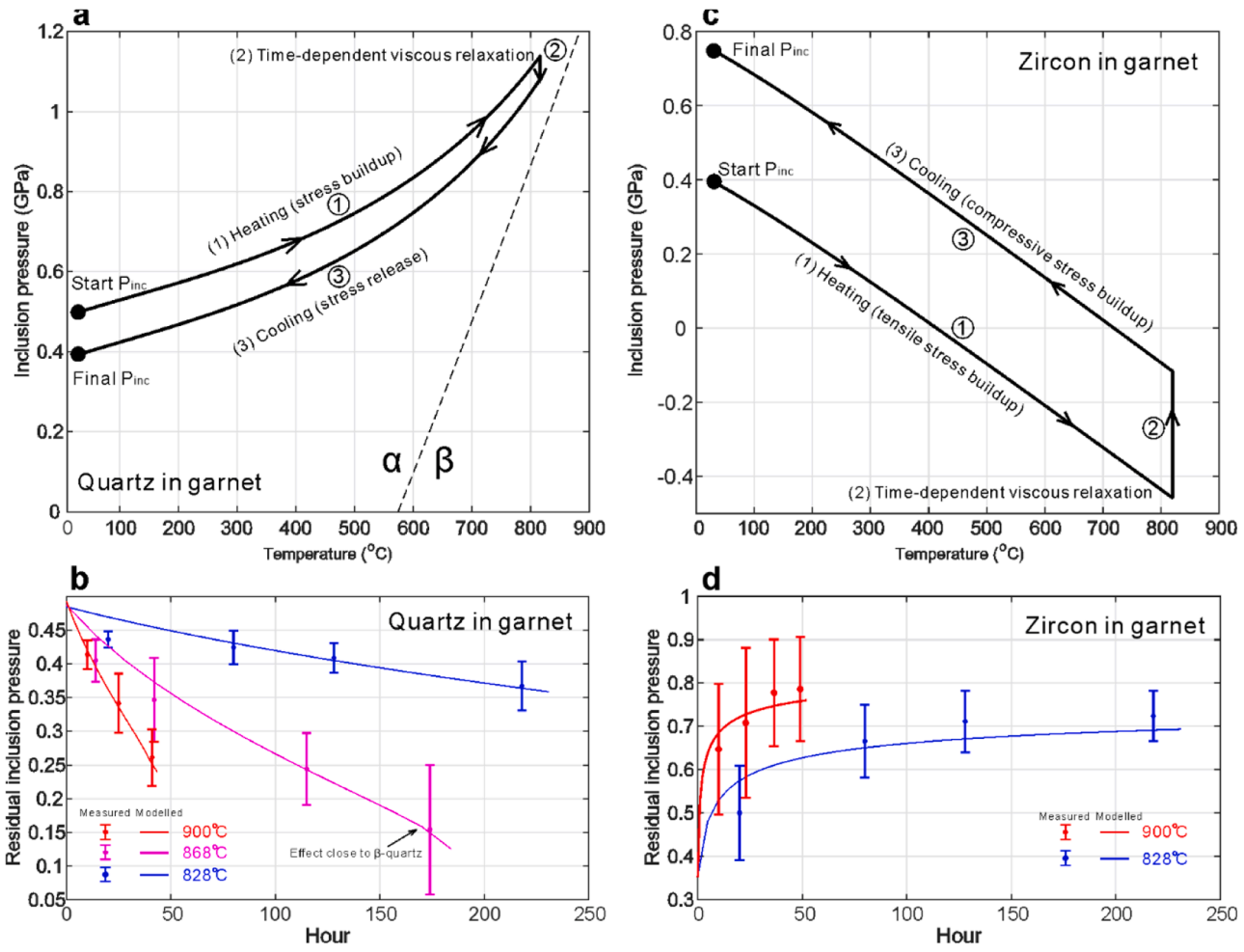

Fig. 7. **a.** Modelled quartz inclusion pressure in a garnet host against temperature as an example. The initial quartz inclusion pressure is 0.5 GPa. The confining pressure is 1 bar. The inclusion-host system is heated to 820 °C at room *P*. The inclusion pressure builds up due to different thermal expansivities between the inclusion and host. At peak-*T*, the inclusion pressure relaxes as a function of time, leading to a lower final residual inclusion pressure. The heating time is 300 h using the given flow law in Table 1. **b.** The measured average residual pressure (points with error bars) and numerically modelled residual pressure (curves) using the best-fitted pre-factor *A* (Table 1) with an assumed stress exponent $n = 3$. **c** and **d** are similar to **a** and **b** but for zircon inclusions initially at 0.4 GPa. Zircon first experiences a transition from compressive to tensile stress due to heating and the tensile stress relaxes, leading to a "viscous pressurization" effect. The residual inclusion pressure is calculated using the published calibration curve given in the main text. The error bars in **b** and **d** are obtained from multiple inclusions as shown in Fig. 3, and the error is propagated into the pre-factor *A* using the bootstrap method.

the residence time of aqueous fluid, if any, is shorter than the characteristic relaxation timescale. For zircon inclusions, viscous relaxation of the pressure is much faster (Fig. 8). In Campomenosi et al. (2023), this is explained to be due to that garnet is weaker under tensile stress, which leads the zircon to reset during isothermal decompression.

On the other hand, our experimental results imply that quartz inclusions entrapped along the prograde path can undergo viscous resetting in the presence of fluids during progressive metamorphism. For example, if a quartz inclusion is entrapped along the prograde *P-T* path, e.g., on entering the stability field of garnet, it may develop an underpressure due to its greater compressibility during the prograde *P-T* evolution. Viscous resetting may also affect those underpressurized quartz inclusions at peak *P-T* conditions, leading to an apparent overstepping effect (Zhong et al., 2020). The difference in pressures estimated by quartz-inclusion elastic barometry and phase-equilibrium modelling has been used to invoke that garnet reaction boundary needs to be overstepped to crystalize garnet (Castro and Spear, 2017). Our results suggested that if fluid was produced from the breakdown of hydrous minerals or external fluid enters during subduction, partial viscous resetting may occur that results in a higher apparent entrapment pressure for quartz inclusions. Examination of isotope chemistry of prograde/retrograde minerals (e.g. Bovay et al., 2021) or μm-sized inclusion's mineralogy (e.g. Spengler et al., 2023) may provide information on the *P-T* condition of fluid infiltration.

Furthermore, our experimental results of quartz inclusions also give insights into metamorphic conditions that lead to the preservation of coesite inclusions in garnet. Natural coesite-bearing samples often exhibit almost no spectroscopic signal from the hydroxyl band (e.g., Katayama et al., 2006; Rossman and Smyth, 1990), although synthetic coesite may contain tens to hundreds of parts per million of water (Koch-Müller et al., 2001; Yan et al., 2021). It has long been recognized that coesite, if perfectly sealed in a garnet host, may experience an overpressure compared to the lithostatic pressure along the coesite-quartz transition curve until a low temperature is reached that hinders the reaction kinetics (Gillet et al., 1984; Parkinson, 2000). However, this analysis is based on consideration that the inclusion and host are in elastic regime. If water is present inside the garnet during the retrograde evolution, the overpressure in the inclusion would be rapidly relaxed. Then the transition will only depend on the reaction kinetics from coesite to quartz, which again can be fast under wet conditions (Lathe et al., 2005; Perrillat et al., 2003). Therefore, the results may explain the dry nature of the surviving coesite inclusions, not only from

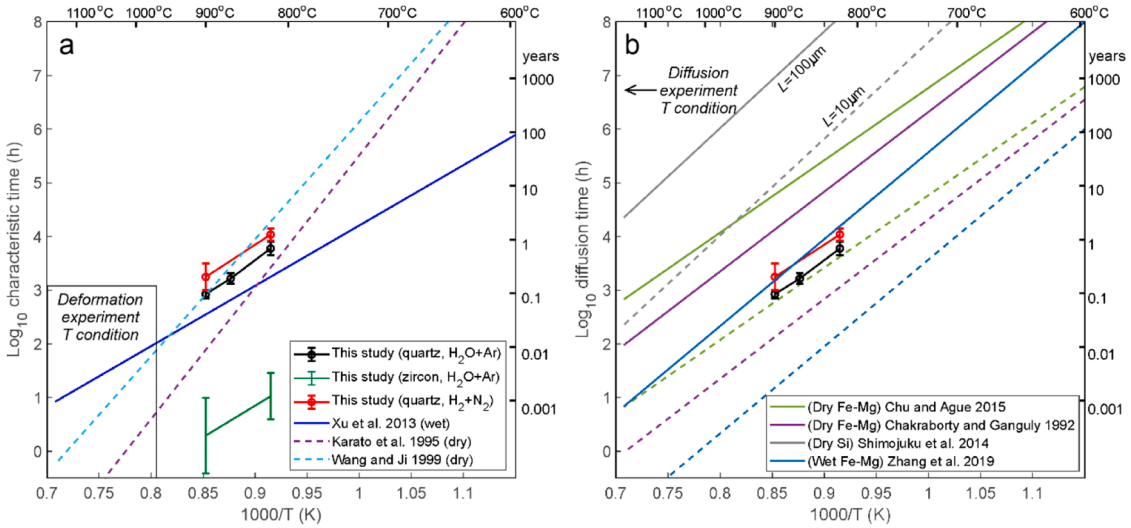

Fig. 8. a. Characteristic timescales of viscous relaxation as functions of temperature for inclusions of quartz and zircon. The flow laws for dry garnet from Karato et al. (1995) and Wang and Ji (1999) and wet garnet from Xu et al. (2013) are shown. For the flow law for wet garnet, the water fugacity is set to 10^4 Pa, and confining pressure is set to 1 bar for comparison with our experimental results. The inclusion pressure is set to 1 GPa. The uncertainty is calculated with a Monte-Carlo method. Alm-Prp garnet flow law is taken from Karato et al. (1995) and Wang and Ji (1999). **b.** Diffusion timescale ($t = L^2/D$, with $L = 100$ μm as solid lines and $L = 10$ μm as dashed lines) as functions of temperature. The diffusion coefficients for Fe-Mg exchange in dry garnet are from Chakraborty and Ganguly (1992); Chu and Ague (2015). Si trace diffusion is from Shimojuku et al. (2014) and that of Fe-Mg diffusion is wet garnet is from Zhang et al. (2019). Confining pressure is set at 1 bar for comparison with timescale of viscous relaxation.

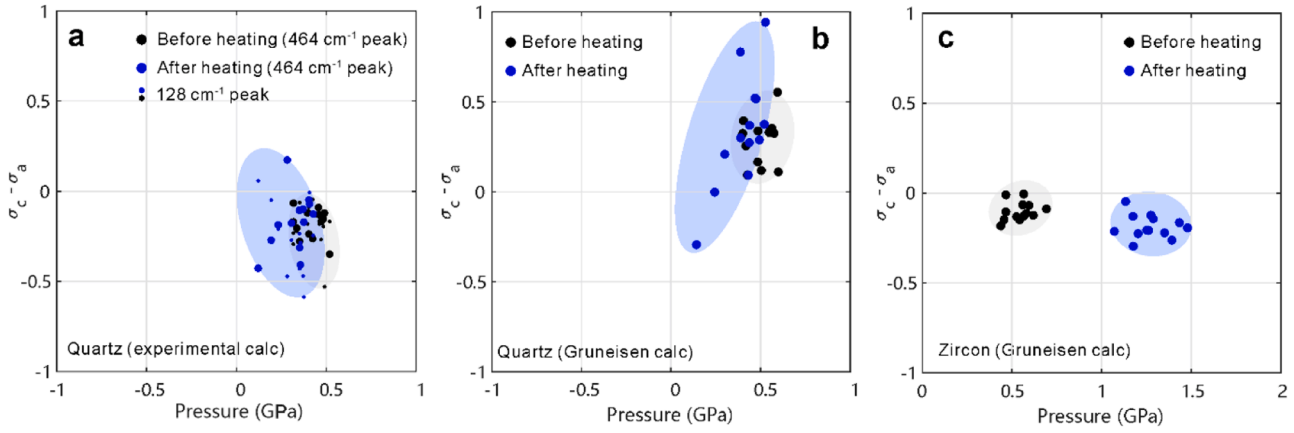

Fig. 9. Calculated pressure and differential stress of quartz (**a** and **b**) and zircon inclusions (**c**). **a** is calculated with experimental calibration for quartz (Reynard and Zhong, 2023). The large dots are obtained with the 464 cm^{-1} peak, and the small dots are with the 128 cm^{-1} peak and the pressure is obtained with the 206 cm^{-1} peak, which is insensitive to nonhydrostatic stress. **b** is calculated with the Grüneisen tensor for quartz (Murri et al., 2018). **c** is calculated with the Grüneisen tensor for zircon (Stangarone et al., 2019). The experiment is performed at 820 °C with H_2O+Ar buffer condition. The black and blue dots represent before and after heating for 218 h, respectively. The used Raman peaks for quartz are 128, 206 and 464 cm^{-1} and for zircon are 439, 975 and 1008 cm^{-1}.

the perspective of reaction kinetics, but also from the mechanical perspective.

Lastly, the flow law is a key component in geodynamic modelling and geophysical exploration (Bürgmann and Dresen, 2008; Kaatz et al., 2023) and is often determined by deformation experiments and geophysical observations (e.g., Karato and Wu, 1993). As we have shown here, the use of inclusion-host systems for studying the time-dependent creep processes of single crystals provides a useful alternative for investigating the rheological behaviour of earth materials. In this work, the furnace is used to control buffering environment. However, the lab-intensive nature of furnace setup may limit the number of datasets that can be collected. An alternative approach is to perform the experiment with a heating stage, similar to the work by Campomenosi et al. (2023), but with different controlled buffer such as water, hydrogen, CO—CO_2, etc., or a diamond anvil cell to add pressure so that the inclusion overpressure can be better controlled. An advantage of such heating experiments is that they can be performed for longer durations. Then the need for measuring stress and strain (rate) with mechanical instruments is in principle replaced by spectroscopic measurements, such as Raman spectroscopy. The variety of mineral inclusion-host pairs (Kohn, 2014) also provides a wide range of difference in thermal expansivity that allows compressive as well as tensile stress to be applied to single crystals. The determined strengths of minerals may also be useful in larger scale geophysical problems and geodynamic modelling.

5. Conclusions

We performed heating experiments on natural inclusion-host systems under graphite buffered, N_2+H_2 fluxed and H_2O+Ar fluxed conditions. In the experiment fluxed with aqueous fluid, time-dependent stress relaxation occurred, indicating that aqueous fluid is an important

factor that weaken the garnet. In graphite buffered experiments, only a small amount of stress relaxation occurs during the first heating step and is negligible thereafter, even at 900 °C, implying that the garnet can be a strong pressure vessel under dry conditions. Raman maps of garnet hosts surrounding quartz inclusions reveal first an increase and then a decrease of spatial heterogeneity in shift magnitudes and the pattern shows a progressive dispersal away from the garnet. Misorientation maps based on EBSD data exhibit patterns with a higher dislocation density for heated samples compared to unheated ones. Numerical modelling provides the garnet viscosity and activation energy under wet conditions. The resulting timescale and activation energy are consistent with previous studies. The characteristic viscous relaxation timescale is compared to diffusion homogenization timescales based on published data. The results indicate that under H_2O+Ar fluxed conditions, both diffusion and stress relaxation occur rapidly, leading to complete chemical and mechanical resetting. Under dry conditions, stress relaxation can be slow, leading to the preservation of stress at high temperature. The determined flow-law parameters can be useful in geodynamic modelling and may provide an alternative to study the long-term rheology of single-crystal minerals.

CRediT authorship contribution statement

Xin Zhong: Project administration, Methodology, Investigation, Funding acquisition, Formal analysis, Data curation, Conceptualization, Resources, Software, Supervision, Validation, Visualization, Writing – original draft, Writing – review & editing. **David Wallis:** Data curation, Investigation, Writing – review & editing. **Phillip Kingsbery:** Data curation, Investigation, Writing – review & editing. **Timm John:** Funding acquisition, Writing – review & editing.

Declaration of competing interest

The authors declare that they have no known competing financial interests or personal relationships that could have appeared to influence the work reported in this paper.

Data availability

The data used to reproduce the figures can be found in supplementary excel sheet.

Acknowledgements

We thank two anonymous reviewers for their helpful comments and Alex Webb for editorial handling. XZ acknowledges the Alexander von Humboldt Foundation and the EXCITE Network for financial support. DW acknowledges support from a UK Research and Innovation Future Leaders Fellowship [grant number MR/V021788/1]. Moritz Liesegang is acknowledged for EPMA analysis. Sumit Chakraborty is acknowledged for helpful comments on discussion from a mechanistic view. Jörg Hermann, Mona Lueder and Julien Reynes are acknowledged for discussions on experiments.

Supplementary materials

Supplementary material associated with this article can be found, in the online version, at doi:10.1016/j.epsl.2024.118713.

References

Angel, R.J., Alvaro, M., Miletich, R., Nestola, F., 2017a. A simple and generalised P–T–V EoS for continuous phase transitions, implemented in EosFit and applied to quartz. Contrib. to Mineral. Petrol. 172, 1–15. https://doi.org/10.1007/s00410-017-1349-x.

Angel, R.J., Gilio, M., Mazzucchelli, M., Alvaro, M., 2022. Garnet EoS : a critical review and synthesis. Contrib. to Mineral. Petrol. 177, 1–22. https://doi.org/10.1007/s00410-022-01918-5.

Angel, R.J., Mazzucchelli, M.L., Alvaro, M., Nestola, F., 2017b. EosFit-Pinc: A simple GUI for host-inclusion elastic thermobarometry. Am. Mineral. 102, 1957–1960. https://doi.org/10.2138/am-2017-6190.

Ashley, K.T., Steele-MacInnis, M., Caddick, M.J., 2014. QuIB Calc: A MATLAB script for geobarometry based on Raman spectroscopy and elastic modeling of quartz inclusions in garnet. Comput. Geosci. 66, 155–157. https://doi.org/10.1016/j.cageo.2014.01.005.

Austrheim, H., 1987. Eclogitization of lower crustal granulites by fluid migration through shear zones. Earth Planet. Sci. Lett. 81, 221–232. https://doi.org/10.1016/0012-821X(87)90158-0.

Bachmann, F., Hielscher, R., Schaeben, H., 2010. Texture analysis with MTEX- Free and open source software toolbox. Solid State Phenom 160, 63–68. https://doi.org/10.4028/www.scientific.net/SSP.160.63.

Baldwin, S.L., Schönig, J., Gonzalez, J.P., Davies, H., von Eynatten, H., 2021. Garnet sand reveals rock recycling processes in the youngest exhumed high- And ultrahigh-pressure terrane on Earth. Proc. Natl. Acad. Sci. U. S. A. 118 https://doi.org/10.1073/pnas.2017231118.

Bale, C.W., Bélisle, E., Chartrand, P., Decterov, S.A., Eriksson, G., Gheribi, A.E., Hack, K., Jung, I.H., Kang, Y.B., Melançon, J., Pelton, A.D., Petersen, S., Robelin, C., Sangster, J., Spencer, P., Van Ende, M.A., 2016. FactSage thermochemical software and databases, 2010-2016. Calphad Comput. Coupling Phase Diagrams Thermochem. 54, 35–53. https://doi.org/10.1016/j.calphad.2016.05.002.

Bayet, L., Agard, P., John, T., Menneken, M., Tan, Z., Gao, J., 2020. Tectonic evolution of the Tianshan Akeyazi metamorphic complex (NW China). Lithos 354–355, 105273. https://doi.org/10.1016/j.lithos.2019.105273.

Bayet, L., John, T., Agard, P., Gao, J., Li, J.L., 2018. Massive sediment accretion at ~80 km depth along the subduction interface: Evidence from the southern Chinese Tianshan. Geology 46, 495–498. https://doi.org/10.1130/G40201.1.

Bonazzi, M., Tumiati, S., Thomas, J., Angel, R.J., Alvaro, M., 2019. Assessment of the reliability of elastic geobarometry with quartz inclusions. Lithos 350–351, 105201. https://doi.org/10.1016/j.lithos.2019.105201.

Bovay, T., Rubatto, D., Lanari, P., 2021. Pervasive fluid-rock interaction in subducted oceanic crust revealed by oxygen isotope zoning in garnet. Contrib. to Mineral. Petrol. 176, 1–22. https://doi.org/10.1007/s00410-021-01806-4.

Bürgmann, R., Dresen, G., 2008. Rheology of the Lower Crust and Upper Mantle: Evidence from Rock Mechanics, Geodesy, and Field Observations. Annu. Rev. Earth Planet. Sci. 36, 531–567. https://doi.org/10.1146/annurev.earth.36.031207.124326.

Campomenosi, N., Angel, R.J., Alvaro, M., Mihailova, B., 2023. Resetting of zircon inclusions in garnet : Implications for elastic thermobarometry 51, 23–27. doi:10.1130/G50431.1/5733973/g50431.pdf.

Castro, A.E., Spear, F.S., 2017. Reaction overstepping and re-evaluation of peak P–T conditions of the blueschist unit Sifnos, Greece: implications for the Cyclades subduction zone. Int. Geol. Rev. 59, 548–562. https://doi.org/10.1080/00206814.2016.1200499.

Chakraborty, S., Ganguly, J., 1992. Cation diffusion in aluminosilicate garnets: experimental determination in spessartine-almandine diffusion couples, evaluation of effective binary diffusion coefficients, and applications. Contrib. to Mineral. Petrol. 111, 74–86. https://doi.org/10.1007/BF00296579.

Chu, X., Ague, J.J., 2015. Analysis of experimental data on divalent cation diffusion kinetics in aluminosilicate garnets with application to timescales of peak Barrovian metamorphism. Scotland. Contrib. to Mineral. Petrol. 170, 1–27. https://doi.org/10.1007/s00410-015-1175-y.

Cisneros, M., Behr, W.M., Platt, J.P., Anczkiewicz, R., 2022. Quartz-in-garnet barometry constraints on formation pressures of eclogites from the Franciscan Complex. California. Contrib. to Mineral. Petrol. 177, 1–23. https://doi.org/10.1007/s00410-021-01876-4.

Dabrowski, M., Powell, R., Podladchikov, Y., 2015. Viscous relaxation of grain-scale pressure variations. J. Metamorph. Geol. 33, 859–868. https://doi.org/10.1111/jmg.12142.

Ehlers, A., Zaffiro, G., Angel, R.J., Boffa Ballaran, T., Carpenter, M.A., Alvaro, M., Ross, N., 2022. Thermoelastic properties of zircon: implications for geothermobarometry. Am. Mineral. 1–27.

Enami, M., Nishiyama, T., Mouri, T., Nami, M.A.E., Ishiyama, T.A.N., Ouri, T.A.M., 2007. Laser Raman microspectrometry of metamorphic quartz: A simple method for comparison of metamorphic pressures. Am. Mineral. 92, 1303–1315. https://doi.org/10.2138/am.2007.2438.

Fei, H., Katsura, T., 2020. Pressure Dependence of Proton Incorporation and Water Solubility in Olivine. J. Geophys. Res. Solid Earth 125, 1–13. https://doi.org/10.1029/2019JB018813.

Gilio, M., Scambelluri, M., Angel, R.J., Alvaro, M., 2022. The contribution of elastic geothermobarometry to the debate on HP versus UHP metamorphism. J. Metamorph. Geol. 40, 229–242. https://doi.org/10.1111/jmg.12625.

Gillet, P., Ingrin, J., Chopin, C., 1984. Coesite in subducted continental crust : P - T history deduced from an elastic model. Earth Planet. Sci. Lett. 70, 426–436.

Gonzalez, J.P., Mazzucchelli, M.L., Angel, R.J., Alvaro, M., 2021. Elastic Geobarometry for Anisotropic Inclusions in Anisotropic Host Minerals: Quartz-in-Zircon. J. Geophys. Res. Solid Earth 126, e2021JB022080. https://doi.org/10.1029/2021jb022080.

Groß, P., Handy, M.R., John, T., Pestal, G., Pleuger, J., 2020. Crustal-Scale Sheath Folding at HP Conditions in an Exhumed Alpine Subduction Zone (Tauern Window, Eastern Alps). Tectonics 39, e2019TC005942. https://doi.org/10.1029/2019TC005942.

Guiraud, M., Powell, R., 2006. P-V-T relationships and mineral equilibria in inclusions in minerals. Earth Planet. Sci. Lett. 244, 683–694. https://doi.org/10.1016/j.epsl.2006.02.021.

Kaatz, L., Reynes, J., Hermann, J., John, T., 2022. How fluid infiltrates dry crustal rocks during progressive eclogitization and shear zone formation: insights from H2O contents in nominally anhydrous minerals. Contrib. to Mineral. Petrol. 177, 72. https://doi.org/10.1007/s00410-022-01938-1.

Kaatz, L., Schmalholz, S.M., John, T., 2023. Numerical Simulations Reproduce Field Observations Showing Transient Weakening During Shear Zone Formation by Diffusional Hydrogen Influx and H 2 O Inflow. Geochemistry, Geophys. Geosystems 24, e2022GC010830. https://doi.org/10.1029/2022GC010830.

Karato, S., Wang, Z., Liu, B., Fujino, K., 1995. Plastic deformation of garnet: systematics and implications for the rheology of the mantle transition zone. Earth Planet. Sci. Lett. 130, 13–20.

Karato, S., Wu, P., 1993. Rheology of the upper mantle: a synthesis. Science (80-.) 260, 771–778. https://doi.org/10.1126/science.260.5109.771.

Karato, S.I., 2012. Deformation of Earth Materials: An Introduction to the Rheology of Solid Earth. Cambridge University Press.

Katayama, I., Nakashima, S., Yurimoto, H., 2006. Water content in natural eclogite and implication for water transport into the deep upper mantle. Lithos 86, 245–259. https://doi.org/10.1016/j.lithos.2005.06.006.

Koch-Müller, M., Fei, Y., Hauri, E., Liu, Z., 2001. Location and quantitative analysis of OH in coesite. Phys. Chem. Miner. 28, 693–705. https://doi.org/10.1007/s002690100195.

Kohlstedt, D.L., 2006. The role of water in high-temperature rock deformation. Water Nominally Anhydrous Miner 62, 377–396. https://doi.org/10.2138/rmg.2006.62.16.

Kohn, M.J., 2014. "Thermoba-Raman-try": Calibration of spectroscopic barometers and thermometers for mineral inclusions. Earth Planet. Sci. Lett. 388, 187–196. https://doi.org/10.1016/j.epsl.2013.11.054.

Kröger, F.A., Vink, H.J., 1956. Relations between the Concentrations of Imperfections in Crystalline Solids. Solid State Phys. - Adv. Res. Appl. 3, 307–435. https://doi.org/10.1016/S0081-1947(08)60135-6.

Lathe, C., Koch-Müller, M., Wirth, R., van Westrenen, W., Mueller, H.J., Schilling, F., Lauterjung, J., 2005. The influence of OH in coesite on the kinetics of the coesite-quartz phase transition. Am. Mineral. 90, 36–43. https://doi.org/10.2138/am.2005.1662.

Mazzucchelli, M.L., Burnley, P., Angel, R.J., Morganti, S., Domeneghetti, M.C., Nestola, F., Alvaro, M., 2018. Elastic geothermobarometry: Corrections for the geometry of the host-inclusion system. Geology 46, 1–4. https://doi.org/10.1130/G39807.1.

Mazzucchelli, M.L., Reali, A., Morganti, S., Angel, R.J., Alvaro, M., 2019. Elastic geobarometry for anisotropic inclusions in cubic hosts. Lithos 350–351, 105218. https://doi.org/10.1016/j.lithos.2019.105218.

Moulas, E., Kostopoulos, D., Podladchikov, Y., Chatzitheodoridis, E., Schenker, F.L., Zingerman, K.M., Pomonis, P., Tajčmanová, L., 2020. Calculating pressure with elastic geobarometry: A comparison of different elastic solutions with application to a calc-silicate gneiss from the Rhodope Metamorphic Province. Lithos 378–379, 105803. https://doi.org/10.1016/j.lithos.2020.105803.

Murri, M., Mazzucchelli, M.L., Campomenosi, N., Korsakov, A.V., Prencipe, M., Mihailova, B.D., Scambelluri, M., Angel, R.J., Alvaro, M., 2018. Raman Elastic Geobarometry For Anisotropic Mineral Inclusions. Am. Mineral. 113, 1869–1872. https://doi.org/10.2138/am-2018-6625CCBY.

Nye, J., 1953. Some geometrical relations in dislocated crystals. Acta Metall 1, 153–162. https://doi.org/10.1016/0001-6160(53)90054-6.

Parkinson, C.D., 2000. Coesite inclusions and prograde compositional zonation of garnet in whiteschist of the HP-UHPM Kokchetav massif, Kazakhstan: A record of progressive UHP metamorphism. Lithos 52, 215–233. https://doi.org/10.1016/S0024-4937(99)00092-4.

Perrillat, J.P., Daniel, I., Lardeaux, J.M., Cardon, H., 2003. Kinetics of the Coesite–Quartz Transition: Application to the Exhumation of Ultrahigh-Pressure Rocks. J. Petrol. 44, 773–788. https://doi.org/10.1093/petrology/44.4.773.

Putnis, A., John, T., 2010. Replacement processes in the earth's crust. Elements 6, 159–164. https://doi.org/10.2113/gselements.6.3.159.

Reynard, B., Zhong, X., 2023. Quartz under stress: Raman calibration and applications of metamorphic inclusions to geobarometry. Solid Earth 14, 591–602. https://doi.org/10.5194/se-14-591-2023.

Rosenfeld, J.L., Chase, A.B., 1961. Pressure and temperature of crystallization from elastic effects around solid inclusions in minerals? Am. J. Sci. https://doi.org/10.2475/ajs.259.7.519.

Rossman, G.R., Smyth, J.R., 1990. Hydroxyl contents of accessory minerals in mantle eclogites and related rocks. Am. Mineral. 75, 775–780.

Schmidt, C., Steele-MacInnis, M., Watenphul, A., Wilke, M., 2013. Calibration of zircon as a Raman spectroscopic pressure sensor to high temperatures and application to water-silicate melt systems. Am. Mineral. 98, 643–650. https://doi.org/10.2138/am.2013.4143.

Schmidt, C., Ziemann, M.A., 2000. In situ Raman spectroscopy of quartz: A pressure sensor for hydrothermal diamond-anvil cell experiments at elevated temperatures. Am. Mineral. 85, 1725–1734. https://doi.org/10.2138/am-2000-11-1216.

Schwarzenbach, E.M., Zhong, X., Caddick, M.J., Schmalholz, S.M., Menneken, M., Hecht, L., John, T., 2021. On exhumation velocities of high-pressure units based on insights from chemical zoning in garnet (Tianshan, NW China). Earth Planet. Sci. Lett. 570, 117065 https://doi.org/10.1016/j.epsl.2021.117065.

Shimojuku, A., Kubo, T., Kato, T., Yoshino, T., Nishi, M., Nakamura, T., Okazaki, R., Kakazu, Y., 2014. Effects of pressure and temperature on the silicon diffusivity of pyrope-rich garnet. Phys. Earth Planet. Inter. 226, 28–38. https://doi.org/10.1016/j.pepi.2013.11.002.

Spengler, D., Włodek, A., Zhong, X., Loges, A., Cuthbert, S.J., 2023. Retrogression of ultrahigh-pressure eclogite, Western Gneiss Region, Norway. Eur. J. Mineral. 35, 1125–1147. https://doi.org/10.5194/ejm-35-1125-2023.

Stangarone, C., Angel, R.J., Prencipe, M., Campomenosi, N., Mihailova, B., Alvaro, M., 2019. Measurement of strains in zircon inclusions by Raman spectroscopy. Eur. J. Mineral. 31, 685–694. https://doi.org/10.1127/ejm/2019/0031-2851.

Szczepański, J., Zhong, X., Dabrowski, M., Wang, H., Goleń, M., 2021. Combined phase diagram modelling and quartz-in-garnet barometry of HP metapelites from the Kamieniec metamorphic belt (NE bohemian massif). J. Metamorph. Geol. 40, 3–37. https://doi.org/10.1111/jmg.12608.

Taguchi, T., Enami, M., Kouketsu, Y., 2019. Metamorphic record of the Asemi-gawa eclogite unit in the Sanbagawa belt, southwest Japan: Constraints from inclusions study in garnet porphyroblasts. J. Metamorph. Geol. 37, 181–201. https://doi.org/10.1111/jmg.12456.

Thomas, J.B., Spear, F.S., 2018. Experimental study of quartz inclusions in garnet at pressures up to 3.0 GPa: evaluating validity of the quartz-in-garnet inclusion elastic thermobarometer. Contrib. to Mineral. Petrol. 173, 1–14. https://doi.org/10.1007/s00410-018-1469-y.

Wallis, D., Hansen, L.N., Ben Britton, T., Wilkinson, A.J., 2016. Geometrically necessary dislocation densities in olivine obtained using high-angular resolution electron backscatter diffraction. Ultramicroscopy 168, 34–45. https://doi.org/10.1016/j.ultramic.2016.06.002.

Wang, Z., Ji, S., 1999. Deformation of silicate garnets: Brittle-ductile transition and its geological implications. Can. Mineral. 37, 525–541.

Wayte, G.J., Worden, R.H., Rubie, D.C., Droop, G.T.R., 1989. A TEM study of disequilibrium plagioclase breakdown at high pressure: the role of infiltrating fluid. Contrib. to Mineral. Petrol. 101, 426–437. https://doi.org/10.1007/BF00372216.

Wheeler, J., Mariani, E., Piazolo, S., Prior, D.J., Trimby, P.J., Drury, M.R., 2012. The Weighted Burgers Vector: A quantity for constraining dislocation densities and types using electron backscatter diffraction on 2D sections through crystalline materials. Mater. Sci. Forum 715–716, 732–736. https://doi.org/10.4028/www.scientific.net/MSF.715-716.732.

Xu, L., Mei, S., Dixon, N., Jin, Z., Suzuki, A.M., Kohlstedt, D.L., 2013. Effect of water on rheological properties of garnet at high temperatures and pressures. Earth Planet. Sci. Lett. 379, 158–165. https://doi.org/10.1016/j.epsl.2013.08.002.

Yan, W., Zhang, Y., Ma, Y., He, M., Zhang, L., Sun, W., Wang, C.Y., Liu, X., 2021. Water in coesite: Incorporation mechanism and operation condition, solubility and P-T dependence, and contribution to water transport and coesite preservation. Geosci. Front. 12, 313–326. https://doi.org/10.1016/j.gsf.2020.05.007.

Zhang, B., Li, B., Zhao, C., Yang, X., 2019. Large effect of water on Fe–Mg interdiffusion in garnet. Earth Planet. Sci. Lett. 505, 20–29. https://doi.org/10.1016/j.epsl.2018.10.015.

Zhang, Y., 1998. Mechanical and phase equilibria in inclusion-host systems. Earth Planet. Sci. Lett. 157, 209–222. https://doi.org/10.1016/S0012-821X(98)00036-3.

Zhong, X., Andersen, N.H., Dabrowski, M., Jamtveit, B., 2019. Zircon and quartz inclusions in garnet used for complementary Raman thermobarometry: application to the Holsnøy eclogite, Bergen Arcs, Western Norway. Contrib. to Mineral. Petrol. 174, 50. https://doi.org/10.1007/s00410-019-1584-4.

Zhong, X., Dabrowski, M., Jamtveit, B., 2021. Analytical solution for residual stress and strain preserved in anisotropic inclusion entrapped in an isotropic host. Solid Earth 12, 817–833. https://doi.org/10.5194/se-12-817-2021.

Zhong, X., Dabrowski, M., Jamtveit, B., 2019. Analytical solution for the stress field in elastic half space with a spherical pressurized cavity or inclusion containing eigenstrain. Geophys. J. Int. 216, 1100–1115. https://doi.org/10.1093/gji/ggy447.

Zhong, X., Moulas, E., Tajčmanová, L., 2020. Post-entrapment modification of residual inclusion pressure and its implications for Raman elastic thermobarometry. Solid Earth 11, 223–240. https://doi.org/10.5194/se-11-223-2020.